Precise optical registration of fine-structured electrical sparks and related challenges

Khristina Smaznova,[1,2,*] **Alexandra Khirianova,**[2] **Egor Parkevich,**[2] **Mikhail Medvedev,**[2] **Evgeniya Varaksina,**[2] **Timofey Khirianov,**[2] **Alexander Oginov,**[2] **and Alexandr Selyukov**[1,2,3]

[1]*Moscow Institute of Physics and Technology, Institutskii per. 9, Dolgoprudnyi, Moscow oblast 141700, Russia*
[2]*P.N. Lebedev Physical Institute of the Russian Academy of Sciences, 53 Leninskiy Prospekt, Moscow 119991, Russia*
[3]*Bauman Moscow State Technical University, 5/1 2-ya Baumanskaya St., 105005 Moscow, Russia*
[*]*smaznova.kht@phystech.edu*

Abstract: Fine-structured sparks naturally formed in electrical gas discharges are challenging objects of optical research. The veracity of the spark structure image obtained by laser probing techniques is still a subject for discussion due to possible distortions introduced by the employed optical setup. We thoroughly analyze this issue by simulating the spark image formation and evaluating the effect of the setup response function on the spark pattern quality. The latter turns out to dramatically suffer from the defocusing effect, whereas the spark fine structure is reliably resolved only by optics having a spatial resolution close to several micrometers.

1. Introduction

Formation of fine-structured electrical sparks generated in laboratory gas discharges is an intriguing phenomenon highly relevant in terms of fundamental and applied physics. The existence of the spark fine structure has recently been unveiled in [1–9] by laser probing techniques, implemented in high-performance optical registration systems. In [1–4], laser shadowgrams and interferograms of fine-structured sparks were registered with a spatial resolution better than 5 μm. The sparks were probed by a laser pulse having a duration of $\approx$ 6 ns and a wavelength of 532 nm. In [5,6], the evolution of the spark fine structure was traced with temporal and spatial resolutions of $\sim$ 1 ns and 3–4 μm. Therein, with the employment of a multi-frame optical setup (provides simultaneous interferometry, shadow photography, and schlieren imaging) [7], the spark was probed by a laser pulse with a duration and wavelength of 70 ps and 532 nm, respectively. Processing of the spark interferograms in [6] demonstrated that sparks (with a typical diameter of $\sim$ 100 μm) contain dozens of closely packed filaments of highly ionized plasma, with the filaments being just $\sim$ 10 μm in diameter. Also, the spark microstructure was detected in the spark glow images recorded in [8] by an image intensifier having an exposure time of $\sim$ 40 ns and a spatial resolution better than 5 μm. The spark microstructure has a persistent character and is observed even tens of nanoseconds after the spark initiation in the discharge [9]. So, there is no doubt about the existence of the fine structure of the natural electrical spark, but the veracity of the registered spark patterns is a subject for discussion. In fact, an accurate investigation of such a complex plasma medium as the fine-structured spark is a challenging problem that requires the employment of special procedures for analyzing the results of optical measurements. Indeed, not every optical system is capable of resolving the spark fine structure and providing for reliable registration of the parameters of the light, be it the probing laser radiation transmitted through the spark or the spark glow. The characteristics of the conventional optics employed (see examples in

[6,10]) can be insufficient for correct registration of the spark structure images without distortions. In terms of image formation, a part of the spatial frequencies describing the observed spark structure can be lost due to the finite circular aperture of the objectives employed in the optical setup [11]. In addition, the spark images can be distorted due to the possible defocusing effect (caused by noncoincidence of the object plane of an objective and the output plane of an object, see in [12–16]) and optical aberrations [16]. Thus, the obtained images can be far from the true spark pattern, and, hence, a more rigorous analysis of the obtained spark images is required.

In this paper, we consider in detail probing of the fine-structured spark by 532 nm laser radiation. By modeling the spark image formation in the optical registration system, we evaluate the effect of the system response function on the quality of the registered spark diffraction and phase patterns (observed in laser shadowgrams and interferograms). We show that the spark microstructure is reliably resolved only by optics having a spatial resolution better than several micrometers. Also, it is found out that the defocusing effect is crucial for precise investigation of complex-structured sparks and should be accounted for in the image processing. Our findings reveal extreme difficulties in optical diagnosing of the fine-structured spark and, at the same time, provide a reliable basis for its comprehensive investigation.

2. Diagnosing setup

The diagnosing setup employed in studying the spark discharge formation is schematically presented in Fig. 1(a). For precise probing of the discharge, we created a high-voltage generator triggered by an ignition laser beam with a jitter of $\lesssim 1$ ns [17]. For triggering the generator and probing the spark, we use a Nd: YAG laser (Lotis LS-2151) providing a laser pulse with the energy up to 80 mJ at 1064 nm and 532 nm. The generator is triggered by a 70 mJ beam with both harmonics, delivering through a 75 Ω transmission coaxial line a 25 kV high-voltage pulse with a rise time and duration of 4 ns and 40 ns, respectively. The pulse is applied to a small air-filled discharge gap at atmospheric pressure. The gap is formed by a flat cathode and a pin anode, see Fig. 1(b). The anode is a millimeter-sized metal wire with a diameter of 100 μm. The spark formation starts in the gap after the electrical breakdown, see more in [18]. At some instant, the spark is probed by a ~ 10 mJ laser pulse having a duration, wavelength, and diameter of 70 ps, 532 nm, and ~ 1 cm, respectively.
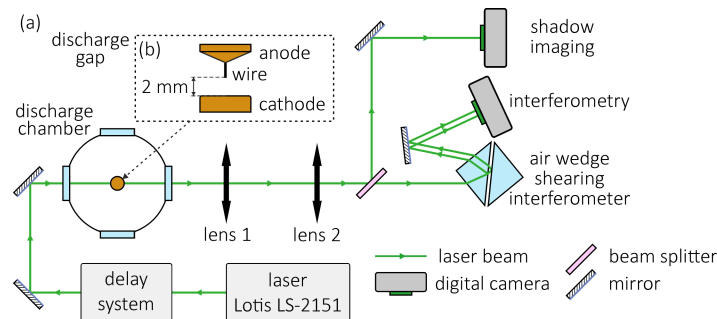
Fig. 1. Schematic representation of the diagnosing setup (a). Studied discharge gap (b) formed by a flat cathode and a pin anode.

The beam transmitted through the spark is collected by lens 1 with additional lens 2 placed behind lens 1. In the setup, lenses 1 and 2 are "Era-14" objectives with focal lengths $F = 135$ mm. At 532 nm, the "Era-14" objective has an ultimate spatial resolution as high as 500 lines/mm ($\approx 91\%$ of the diffraction limit) with a maximum f-number of f/2.8. The entrance and exit pupils of the "Era-14" objective have similar diameters governed by the diameter ($\tilde{D} \approx 48.21$ mm) of the aperture diaphragm. To implement laser probing techniques, a beam splitter (with an

antireflection coating on its back surface) is introduced behind lens 2, in front of its focal plane, to divide the transmitted beam into two beams. One of these beams is involved in shadowgraphy (direct registration of the laser beam), and the other is employed in registering interferograms. The interferograms are obtained by using the beams reflected from the front and back sides of an air wedge between two rectangular glass prisms of a shearing interferometer [7,19–21]. The interferometer is adjusted in the focal plane of lens 2 so that to obtain the object interferograms with high contrast. The spark interferograms and shadowgrams are recorded by digital cameras (Canon EOS 1100D with a CMOS sensor: 22.2×14.7 mm, 12.2 effective megapixels) additionally coupled to green glass filters for attenuating the spark glow. During the discharge probing, the camera shutters are open, so the exposure time of each obtained frame is governed by the duration of the incident laser pulse. The spark images are recorded with a ≈ 6.1× image magnification (*M*). By analyzing the images of the pin electrode in the image plane of lens 2, the magnification is estimated as *M = characteristic pixel size × wire diameter in pixels / wire diameter (100 μm)*. With $M \approx 6.1$, the CMOS sensor captures the entire discharge gap image.

The employed "Era-14" objectives are designed as asymmetrical semi-bonded anastigmats having six lenses in five groups (see in [22]). The main planes of such objective are offset relative to the entrance and exit pupils. When the "Era-14" objective operates as a "long-focus microscope", the focal plane behind the objective is close to the exit pupil. At the same time, the shearing interferometer should be placed exactly in the focal plane. This is the optimal operation regime of the employed interferometer, see in [19–21]. Therefore, an additional lens (lens 2) is introduced behind lens 1. In the setup, lens 1 provides the image magnification of $M \approx 6.1$ whereas lens 2 operates at $M \approx 1$. Owing to the implemented adjustment of the objectives and their high-performance optical characteristics, the introduction of lens 2 behind lens 1 does not degrade the quality of the recorded images (this fact has been proved experimentally). Thus, the characteristics of the employed optical setup are mostly governed by the properties of lens 1.

3. Spark images

Figures 2(a) and 2(b) are the simultaneously registered shadowgram and interferogram of the spark channel with a filamentary structure. Figure 2(c) demonstrates a high-contrast diffraction pattern of the resultant spark channel having a characteristic diameter of ∼ 200 μm. The pattern is extracted from the shadowgram (registered ∼ 10 ns after the gap breakdown) by employing an iterative image denoising procedure developed in [23]. To remove the residual noise in the image, we set to zero the amplitudes of the intensity fluctuations having values less than the average noise amplitude ($I^{noise} \approx 0.2$ arbitrary units). The intensity scale (*I*) describes relative changes in the intensity of the transmitted laser beam, whereas the intensity of the incident beam is taken as unity (normalized intensity of a plane wave). Figure 2(d) is a 2D phase shift map extracted from the interferogram. This map is obtained by employing the algorithm of nonlinear locally adaptive processing of interference images described in [24] and illustrates the phase shift ($\Delta\phi$) introduced by the spark plasma. Phase fluctuations having amplitudes less than the average noise amplitude ($\Delta\phi^{noise} \approx 0.6$ rad) are removed from the map. Figure 3 demonstrates the characteristics (intensity and phase shift distributions) of the transmitted radiation obtained for the slice in Figs. 2(c) and 2(d). The spark diffraction pattern contains multiple fine-scale beats of the image intensity. For the considered slice, the step and FWHM of the beats are within 10–20 μm and 3–7 μm. The average step of the beats is close to 15 μm, and the average FWHM is as low as 5 μm. A twofold increase and a fivefold decrease in the image intensity are observed in some local zones with potential strong overlapping of numerous filaments. The intensity beats correlate with the phase shift beats near the center of the resultant spark channel. Notably, in the considered shot, the phase shift introduced by the filaments at the periphery of the resultant channel turns out to be beyond the sensitivity of the employed single-pass interferometry,

Optics EXPRESS

although in this zone the accumulation of diffraction effects is quite noticeable, which is clearly seen in the radiation intensity distribution.
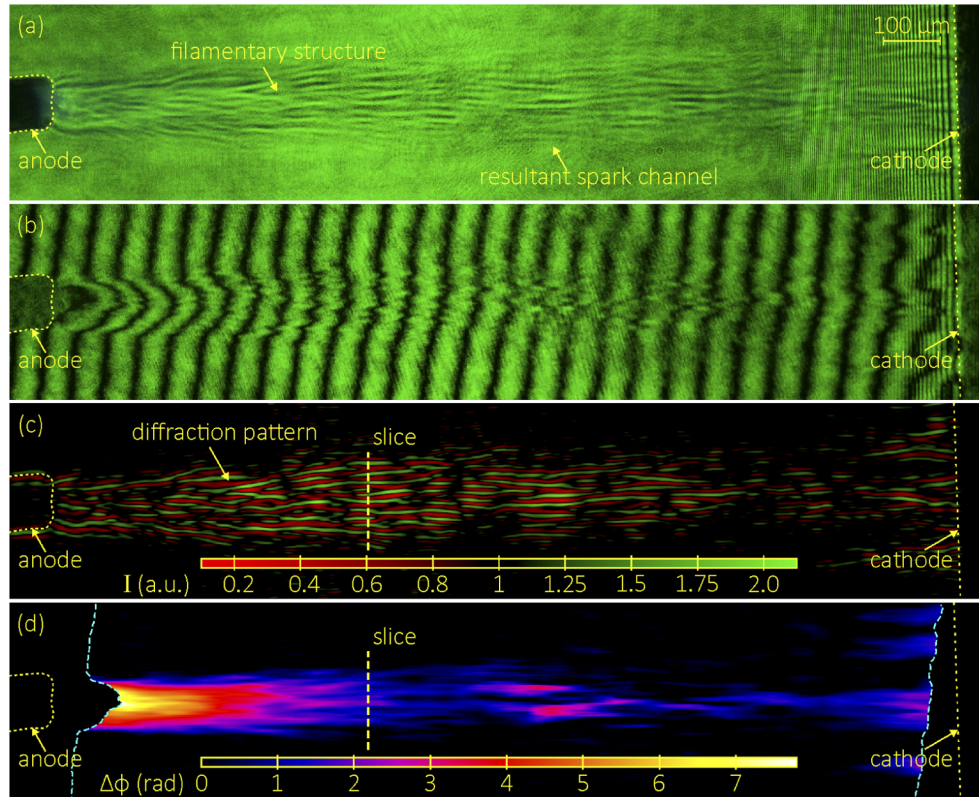
Fig. 2. Spark channel shadowgram (a) and interferogram (b) simultaneously registered ∼ 10 ns after the gap breakdown. Spark diffraction pattern (c) extracted from the shadowgram as illustrated by the changes in the radiation intensity. Map (d) of the phase shift introduced into the transmitted radiation by the spark plasma, extracted from the interferogram. The spark diffraction and phase shift patterns are given in the intensity I and phase shift $\Delta\phi$ scales, characterizing the intensity and phase shift beats having amplitudes larger than the average noise amplitude ($I^{noise} \approx 0.2$ arbitrary units and $\Delta\phi^{noise} \approx 0.6$ rad). The yellow dotted and blue dashed lines indicate the electrode boundary and the trace of the fringe closest to the corresponding electrode, which could be processed correctly.

So, the analysis of the radiation intensity and phase shift distributions indicates that the spark images in Figs. 2(c),(d) are mostly composed of fine-scale structures. In the framework of the image formation theory, these are described by high spatial frequencies in the spatial frequency domain. As noted above, a part of high spatial frequencies can be lost due to the finite bandwidth of the optical system, entailing distortion of the true spark pattern. We will analyze this problem by using the extracted distributions of the radiation intensity and phase shift shown in Fig. 3, relying on their information capacity.
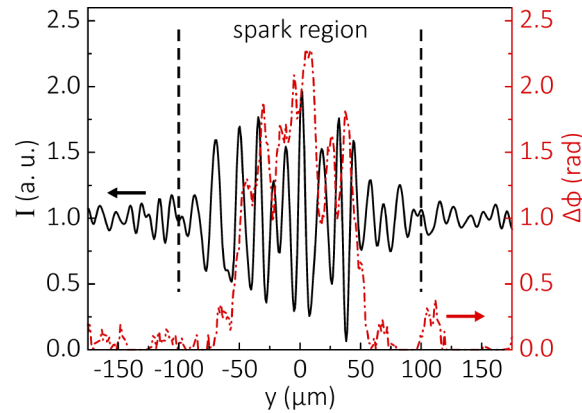
Fig. 3. Intensity (*I*) and phase shift (Δφ) distributions obtained for the slice in Figs. 2(c),(d). The marked spark region is ≈ 200 *μ*m in diameter. The characteristic center of the resultant spark channel is taken as zero in the graphs.

4. Focusing on the spark

In order to evaluate the response function of the optical system, it is convenient to consider an equivalent single-lens system, see Fig. 4, instead of the entire complex setup. The optical characteristics (focal length, pupil diameters, magnification, etc.) of the equivalent lens can be taken similar to those of lens 1. Let us clarify the accuracy of focusing on the developing spark. Notably, here the employment of a pin electrode is of vital importance. Such electrode enhances the local electric field at the electrode surface and facilitates the spark generation in a particular region of the discharge gap. In addition, in the employed discharge gap geometry, the channel develops approximately along the gap axis coinciding with the anode axis. In the experiments, we intentionally adjust lens 1 so that the wire boundary falls within the lens's depth of field ($DOF \approx 1.77\lambda/N.A.^2$ [25]). Parameter λ is the beam wavelength and $N.A. = \sin\alpha = \tilde{D}/2d_0$ is the pupil's numerical aperture on the object side. For the image side, we have $N.A.' = \sin\alpha' = \tilde{D}/2d_i$. The refractive indices of the media in the object and image spaces are equal to unity. Distances d_0 and d_i are measured from the entrance and exit pupils to the object and image planes. These obey the thin-lens formula

$$1/d_0 + 1/d_i - 1/F = 0. \qquad (1)$$

For the specified lens magnification, we have $d_i/d_0 = M \approx 6.1$.
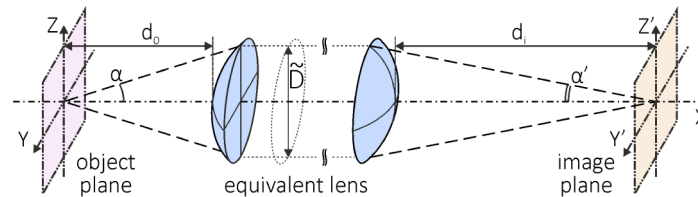
Fig. 4. Equivalent single-lens system. Distances d_0 and d_i are measured from the entrance and exit pupils to the object and image planes, respectively. The entrance and exit pupil diameters are governed by the diameter $\tilde{D}$ of the aperture diaphragm. Parameters α and α' stand for the entrance and exit aperture angles.

It is assumed that the *DOF* value governs the longitudinal size of the region, for which changing the position of the object plane practically does not degrade the quality of the object image. As

known, the increase in *N.A.* improves the lens resolution but reduces *DOF* [25]. In our case
($M \approx 6.1$), parameters *N.A.* and *DOF* are ≈ 0.153 (85% of the theoretical maximum) and ≈ 40
μm. The wire radius is comparable with *DOF*, which allows precise focusing on the wire with
a sharp boundary. Here, one can assume that the object plane coincides with the wire axis.
Meanwhile, the front of the laser beam transmitted through the extended spark is completely
formed in the output plane (Fig. 5), with its position determined by the characteristic boundary
of the fine-structured spark. The object and output planes are assumed to be parallel since the
objective pupil is coaxial with the main optical axis; these planes are separated by distance Δd_0.
Its value can be taken equal to the characteristic radius (100 μm) of the resultant spark channel,
see Fig. 3. The channel boundaries are determined by analyzing the statistical characteristics of
the image intensity in the zones with and without the spark. The data analysis is performed for the
denoised shadowgrams recorded with and without the spark. To this end, in an independent shot,
we have recorded a reference shadowgram with no discharge. The shadowgrams are denoised by
using the image processing technique developed in [23].
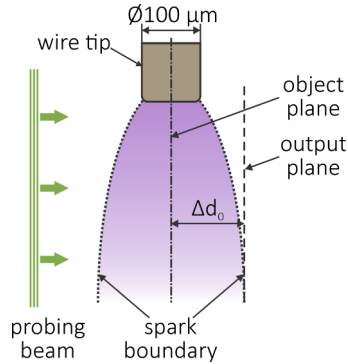
Fig. 5. Schematic of focusing on the spark. The object plane coincides with the wire axis.
The beam front is completely formed in the output plane. The output and object planes are
separated by distance Δd_0.

For the analysis of the characteristics of the transmitted radiation, it is important to reconstruct
them in the output plane exactly. In respect to this plane, the lens turns out to be adjusted so that
we have

$$1/(d_0 - \Delta d_0) + 1/d_i - 1/F > 0. \tag{2}$$

The noncoincidence of the object and output planes essentially entails the defocusing effect [16]
since Eq. (1) is no more valid. The defocusing effect in the object space gives rise to a similar
effect in the image space, and Eq. (1) can be written as

$$1/(d_0 - \Delta d_0) + 1/(d_i + \Delta d_i) - 1/F = 0. \tag{3}$$

By subtracting (1) from (3), we obtain relation

$$\Delta d_i = M^2 \Delta d_0 \tag{4}$$

for quantifying the defocusing effect in the image space. Here one should remember that the
image plane is fixed in the experiment, and the appearing defocusing effect characterizes the
discrepancy between the emergent beam front and the Gauss reference sphere at the considered
point in the image space. We will account for this fact when analyzing the response function of
the lens system.

5. Image formation modeling

Let the radiation transmitted through the spark be described by a wave having complex amplitude $u_0(y, z) = \sqrt{I_0}\exp(i\Delta\phi_0)$. Functions I_0 and $\Delta\phi_0$ are the radiation intensity and phase shift distributions in the object coordinates y and z in the output plane. In the image plane (behind the lens), the wave has amplitude $u_i(y', z') = \sqrt{I}\exp(i\Delta\phi)$. Functions I and $\Delta\phi$ are the radiation intensity and phase shift distributions extracted from the shadowgram and interferogram. These functions are given in the image coordinates y' and z'. The spark image formation in the lens system can be described in the framework of the diffraction theory under the paraxial approximation, employing the concept of canonical object coordinates ($\eta_y = -yN.A./\lambda$, $\eta_z = -zN.A./\lambda$) and canonical image coordinates ($\eta_y' = -y'N.A.'/\lambda$, $\eta_z' = -z'N.A.'/\lambda$) [26,27]. With such coordinates, any lens has 1× magnification and a round pupil of a unit radius, the Fraunhofer diffraction integrals describing the wave transmission in the object and image spaces are expressed as Fourier transforms

$$\tilde{u}_0(\rho_y, \rho_z) = \frac{1}{2\pi}\int_{-\infty}^{+\infty}\int_{-\infty}^{+\infty} u_0(\eta_y, \eta_z)\exp\left[-2\pi i(\eta_y\rho_y + \eta_z\rho_z)\right]d\eta_y d\eta_z, \tag{5}$$

$$\tilde{u}(\rho_y', \rho_z') = \tilde{u}_0(\rho_y, \rho_z)X(\rho_y, \rho_z), \tag{6}$$

$$u_i(\eta_y', \eta_z') = \frac{1}{2\pi}\int_{-\infty}^{+\infty}\int_{-\infty}^{+\infty} \tilde{u}(\rho_y', \rho_z')\exp\left[2\pi i(\eta_y'\rho_y' + \eta_z'\rho_z')\right]d\rho_y' d\rho_z'. \tag{7}$$

Here $u_i(\eta_y', \eta_z')$ and $u_0(\rho_y, \rho_z)$ are the wave amplitudes in the image plane and the output plane; $X(\rho_y, \rho_z)$ is the generalized pupil function given as

$$X(\rho_y, \rho_z) = \begin{cases} \exp\left[-2\pi iW(\rho_y, \rho_z)\right], & \rho_y^2 + \rho_z^2 \le 1 \\ 0, & \rho_y^2 + \rho_z^2 > 1 \end{cases} \tag{8}$$

Function $X(\rho_y, \rho_z)$ is expressed in canonical pupil coordinates and is obtained assuming no diffraction effects at the edges of the aperture diaphragm of the lens. Function $W(\rho_y, \rho_z)$ is the aberration function involving both the geometrical aberrations of the lens and the defocusing effect. Disregarding the geometrical aberrations (owing to the high-performance optical characteristics of the employed objectives), we will associate $W(\rho_y, \rho_z)$ with the defocusing effect only. For the case of the lens focusing on the spark considered in Section 4, the analysis of the defocusing problem according to [12] (see in chapter I) gives the following formula

$$W(\rho_y, \rho_z) = N.A.'^2\Delta d_i(\rho_y^2 + \rho_z^2)/2\lambda. \tag{9}$$

The aberration function can take both positive and negative values, depending on the position of the output plane relative to the object plane. For the case in Fig. 4, as the distance d_0 decreases, the displacement of the image plane leads to an increase in d_i. So, function $W(\rho_y, \rho_z)$ in (9) takes positive values.

By using Eqs. (5)–(9), one can quantify the distortions introduced into the spark image by the optical system, as well as reconstruct the parameters of the transmitted laser beam right in the output plane with account for the defocusing effect.

5.1. Spark pattern in the output plane

The spark pattern reconstruction in the output plane is an incorrect inverse problem since we deal only with that part of the spark pattern preimage, which has passed through the equivalent lens, having the finite bandwidth in the spatial frequency domain. Here we are essentially limited by the spatial resolution of lens 1, and we get nothing better than the distributions in Fig. 3

(in terms of reconstructing finer beats of the radiation intensity and phase shift). However, defocusing can have a strong impact on the quality of the transmitted part of the spark pattern preimage and this circumstance can be accounted for. In Fig. 6, there are the radiation intensity and phase shift distributions reconstructed in the output plane by simulating Eqs. (5)–(9) with $\Delta d_0 = 100 \ \mu$m (our case of the lens focusing on the spark, see Fig. 5). For the fine-structured spark, the defocusing effect entails noticeable changes in the morphology of the radiation intensity distribution, see Fig. 6(a). Locally, the amplitude and shape of some intensity beats are greatly distorted. In Fig. 6(b), pronounced changes in the morphology of the radiation phase shift distribution are also observed. To evaluate the statistical changes in the registered and reconstructed radiation characteristics, we calculate the corresponding relative errors (*RE*) $\delta_I(y_q) = |I(y_q) - I_0(y_q)|/I(y_q)$, $\delta_{\Delta\phi}(y_q) = |\Delta\phi(y_q) - \Delta\phi_0(y_q)|/\Delta\phi(y_q)$, mean relative errors (*MRE*) $\overline{\delta}_I = Q^{-1} \sum_{q=1}^{Q} \delta_I(y_q)$, $\overline{\delta}_{\Delta\phi} = Q^{-1} \sum_{q=1}^{Q} \delta_{\Delta\phi}(y_q)$, maximum relative errors (*RE*$_{\max}$) $\delta_I^{\max}$, $\delta_{\Delta\phi}^{\max}$, as well as root mean square errors (*RMSE*) $\sigma_I = \sqrt{\sum_{q=1}^{Q} \delta_I(y_q)^2/Q}$, $\sigma_{\Delta\phi} = \sqrt{\sum_{q=1}^{Q} \delta_{\Delta\phi}(y_q)^2/Q}$. Functions $I(y_q)$ and $\Delta\phi(y_q)$ are the radiation intensity and phase shift distributions registered in the image plane. Functions $I_0(y_q)$ and $\Delta\phi_0(y_q)$ are the radiation intensity and phase shift distributions reconstructed in the output plane. Parameter Q is the number of the considered points (pixels) in the spark region; y_q stands for the point coordinate. For the intensity and phase shift distributions, the errors are computed for the zones, where the corresponding signal is greater than the average noise amplitude. For the radiation characteristics in Figs. 6(a) and 6(b), we have $\overline{\delta}_I \approx 22\%$, $\overline{\delta}_{\Delta\phi} \approx 8\%$, $\delta_I^{\max} \approx 148\%$, $\delta_{\Delta\phi}^{\max} \approx 59\%$, $\sigma_I \approx 33\%$, $\sigma_{\Delta\phi} \approx 14\%$. The spark pattern veracity dramatically suffers from the defocusing effect in local zones of the spark region, although, in the image plane, the registered intensity and phase shift distributions visually preserve the fine-scale structures of the "true spark pattern". So, to approach the true spark pattern, one should account for the fundamental features of focusing the optical registration system on a complex-structured phase object as well as for the possible noncoincidence of the object plane of the objective and the output plane of the spark.
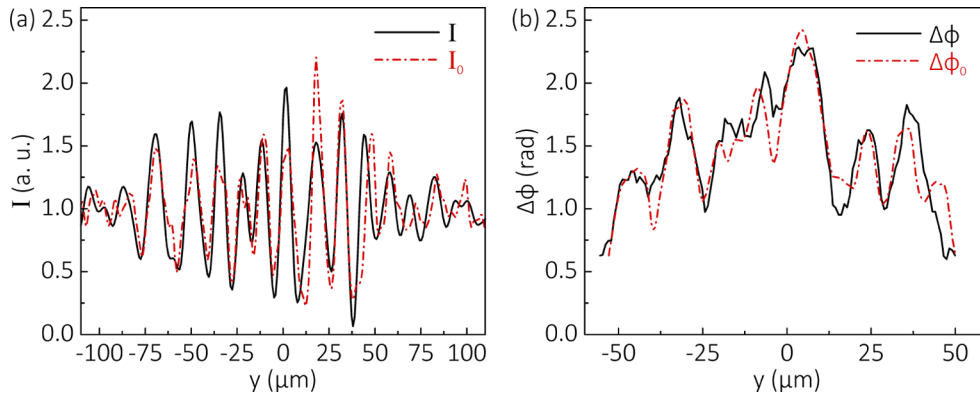
Fig. 6. Radiation intensity distributions (a) registered in the image plane (I) and reconstructed in the output plane (I_0). Radiation phase shift distributions (b) registered in the image plane ($\Delta\phi$) and reconstructed in the output plane ($\Delta\phi_0$).

5.2. Accuracy of reconstructing radiation characteristics

In fact, the boundaries of the resultant spark channel in the images can be determined only with particular accuracy, so can be the position of the output plane. In addition, there can be a slight mismatch between the positions of the object plane and the anode axis. These facts entail a natural spread of the Δd_0 values. Notably, here the effect of the non-parallelism of the object and

output planes on the reconstruction of the radiation characteristics turns out to be no higher than the error (this is <1%) of determining the magnification of the optical system. This fact is owing to precise adjustment of the objectives in the optical setup. So, taking into account the accuracy of focusing the optical system on the anode wire (here we proceed from the observed sharpness of the wire boundaries in the registered interferogram and shadowgram), as well as the accuracy of determining the characteristic boundaries of the resultant spark channel (in the shadowgram), the maximum deviation of the output plane from its most probable position ($\Delta d_0 = 100$ μm) is assumed to be not higher than 20 μm. Hence, it is reasonable to estimate the resultant accuracy of reconstructing the radiation characteristics in the output plane by analyzing the radiation characteristics reconstructed in the planes separated from the object plane by $\Delta d_0 = 80$–120 μm. Here, we will evaluate the statistical discrepancies (described by $\bar{\delta}_I$, $\bar{\delta}_{\Delta\phi}$, $\delta_I^{\max}$, $\delta_{\Delta\phi}^{\max}$, σ_I, $\sigma_{\Delta\phi}$) between the radiation intensity and phase shift distributions reconstructed for different Δd_0 values and those reconstructed with $\Delta d_0 = 100$ μm.

The radiation characteristics reconstructed for $\Delta d_0 = 80$ μm, 100 μm, and 120 μm are demonstrated in Fig. 7. The errors describing the statistical discrepancies for the radiation intensity and phase shift distributions are shown in Fig. 8. Herein, the errors are computed as functions of Δd_0. In the case at hand, $I(y_q)$ and $\Delta\phi(y_q)$ are taken to be the radiation intensity and phase shift distributions reconstructed at $\Delta d_0 = 100$ μm, with $I_0(y_q)$ and $\Delta\phi_0(y_q)$ being the radiation intensity and phase shift distributions reconstructed at $\Delta d_0 = 80$ μm or $\Delta d_0 = 120$ μm. Visually, the obtained radiation characteristics (with $\Delta d_0 = 80$ μm or $\Delta d_0 = 120$ μm) epitomize those reconstructed at $\Delta d_0 = 100$ μm. The shape and position of most intensity and phase shift beats are preserved. The amplitude of the largest beats does not change greatly on average. Locally, with $\Delta d_0 = 80$ μm and $\Delta d_0 = 120$ μm, the maximum discrepancy of the phase shift distributions is described by $\delta_{\Delta\phi}^{\max} \approx 16\%$ and $\approx 19\%$. For the radiation intensity distributions, we have $\delta_I^{\max} \approx 39\%$ and $\approx 31\%$, respectively. On average, the discrepancies are characterized by errors $\bar{\delta}_I \approx 7\%$, $\bar{\delta}_{\Delta\phi} \approx 4\%$ for $\Delta d_0 = 120$ μm and $\bar{\delta}_I \approx 8\%$, $\bar{\delta}_{\Delta\phi} \approx 4\%$ for $\Delta d_0 = 80$ μm, with the root mean square errors being $\sigma_I \approx 10\%$, $\sigma_{\Delta\phi} \approx 5\%$ and $\sigma_I \approx 11\%$, $\sigma_{\Delta\phi} \approx 5\%$. Proceeding from the error values, one can see the similarity of the statistical discrepancies between the radiation characteristics reconstructed at $\Delta d_0 = 80$ μm and 120 μm. Therefore, the described errors can be taken to characterize the resultant accuracy of reconstructing the radiation characteristics in the output plane, with its position distanced from the object plane by $\Delta d_0 = 100$ μm. So, as a rough approximation, the phase shift and intensity distributions are reconstructed in the output plane, with the resultant errors being not higher than $\sim 20\%$ and $\sim 40\%$. These errors characterize the most significant distortions introduced into local zones of the reconstructed spark patterns when taking into account the defocusing effect, although the noted errors are much less on average.

5.3. *Impact of the objective resolution*

The spatial resolution of the employed optics affects the quality of the registered spark patterns as significantly as the defocusing effect does. Let us analyze this issue in detail. Without reducing the generality of the task, we will simulate the direct problem given by Eqs. (5)–(9) for different values of the lens numerical aperture (*N.A.*), assuming no defocusing effect ($\Delta d_0 = 0$) and geometrical aberrations. In accordance with the Rayleigh criterion, the theoretical ultimate spatial resolution of a lens can be estimated as $l \approx 0.61\lambda/N.A.$ For the equivalent lens (with $N.A. = 0.153$) in Fig. 4 and $\lambda = 532$ nm, we have $l \approx 2.1$ μm. In [6,10], it has been experimentally established that no spark microstructure is observed when using conventional optics having a spatial resolution of ~ 10–20 μm. Therefore, it is important to simulate the direct problem with $l = 2.1$–20 μm. To this end, we can use the radiation characteristics in Fig. 6, relying on their information capacity. Recall, these are reconstructed in the output plane with $l = 2.1$ μm. With no defocusing effect, the taken radiation intensity and phase shift distributions are in the
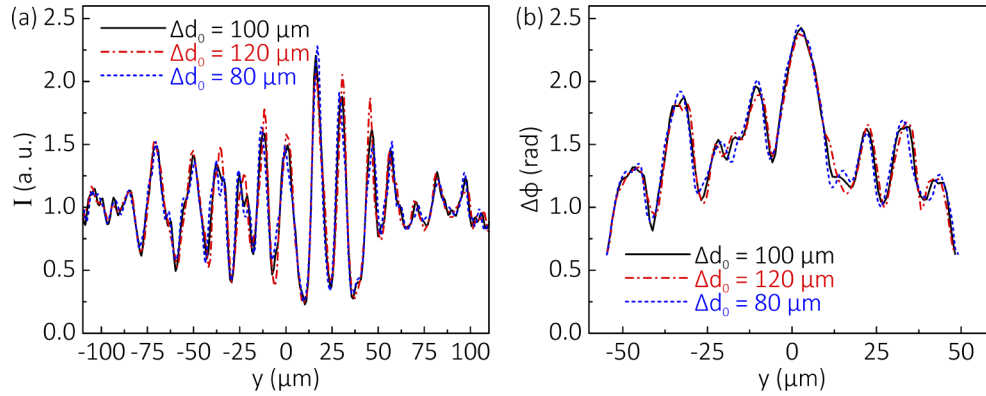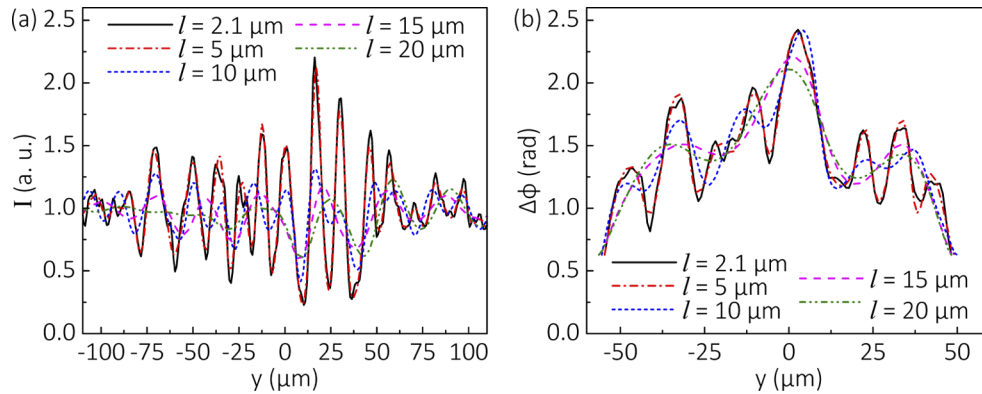
Fig. 7. Radiation intensity (a) and phase shift (b) distributions reconstructed in the planes separated from the object plane by $\Delta d_0 = 80 \ \mu m$, $100 \ \mu m$, and $120 \ \mu m$.
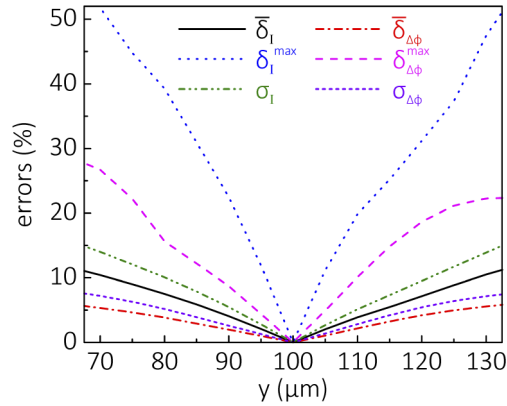
Fig. 8. Mean relative errors ($\overline{\delta}_I$, $\overline{\delta}_{\Delta\phi}$), maximum relative errors (δ_I^{max}, $\delta_{\Delta\phi}^{max}$), and root mean square errors (σ_I, $\sigma_{\Delta\phi}$) as functions of Δd_0. The errors characterize the distortion of the reconstructed spark pattern, which is caused by the possible deviation of the output plane from its most probable position ($\Delta d_0 = 100 \ \mu m$).

object plane; these are constant for both the object plane and the image plane. At the same time, degradation of l distorts the distributions.

In Fig. 9, there are the radiation intensity (I) and phase shift ($\Delta\phi$) distributions simulated in the image plane with $l = 5 \ \mu m$, $10 \ \mu m$, $15 \ \mu m$, and $20 \ \mu m$. To evaluate the statistical discrepancies for the simulated radiation characteristics, we also compute the corresponding errors $\overline{\delta}_I$, $\overline{\delta}_{\Delta\phi}$, δ_I^{max}, $\delta_{\Delta\phi}^{max}$, σ_I, $\sigma_{\Delta\phi}$, see Fig. 10. Here, each intensity and phase shift distribution simulated with a particular value of $l > 2.1 \ \mu m$ is compared with that obtained at $l = 2.1 \ \mu m$ (reconstructed in the output plane, Fig. 6). So, the degradation of the lens resolution results in significant smoothing of the intensity and phase shift beats. With $l = 3.5$–$5 \ \mu m$, the simulated radiation characteristics are approximately similar to the basic radiation characteristics reconstructed in the output plane, but the local discrepancies of the characteristics are increased. For $l = 5 \ \mu m$, the maximum discrepancies between the simulated intensity and phase shift distributions and the basic ones are less than $\delta_I^{max} \approx 28\%$ and $\delta_{\Delta\phi}^{max} \approx 16\%$. On average, the discrepancies are characterized by the errors $\overline{\delta}_I \approx 6\%$ and $\overline{\delta}_{\Delta\phi} \approx 3\%$, with the root mean square errors being $\sigma_I \approx 8\%$ and $\sigma_{\Delta\phi} \approx 4\%$. With $l = 10 \ \mu m$, the discrepancies are greatly increased, and we have $\delta_I^{max} \sim 157\%$, $\delta_{\Delta\phi}^{max} \sim 45\%$,

Fig. 9. Radiation intensity (a) and phase shift (b) distributions simulated in the image plane for different values of the lens spatial resolution (l), assuming no defocusing effect and geometrical aberrations.

$\overline{\delta}_I \approx 23\%$, $\overline{\delta}_{\Delta\phi} \approx 10\%$, $\sigma_I \approx 35\%$, $\sigma_{\Delta\phi} \approx 13\%$. The profile of the phase shift is dramatically smoothed, and the phase shift beats are poorly resolved. The same applies to the intensity beats, the amplitude of which is significantly decreased. The spark diffraction pattern simulated with $l = 10$ μm is so distorted that one can expect very poor visualization of the spark structure in the initial shadowgram (registered in the experiment and not denoised) due to the significant decrease in the spark contrast. Further degradation of the lens resolution (see the intensity and phase shift distributions simulated with $l = 15$ μm and 20 μm) entails dramatic smoothing of the intensity and phase shift beats in the image plane, and the spark pattern itself is distorted so much that correct registration of the spark microstructure becomes impossible. This fact correlates with the unobservability of the spark structure when using conventional optics. Apart from low spatial resolution, the latter suffer from geometrical aberrations, which make the registered spark pattern even more distorted.
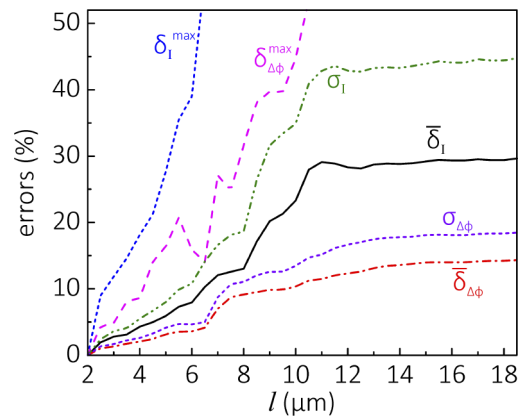
Fig. 10. Mean relative errors ($\overline{\delta}_I$, $\overline{\delta}_{\Delta\phi}$), maximum relative errors ($\delta_I^{\max}$, $\delta_{\Delta\phi}^{\max}$), and root mean square errors (σ_I, $\sigma_{\Delta\phi}$) as functions of the lens spatial resolution (l). The errors describe the discrepancy between the simulated intensity and phase shift distributions and those (Fig. 6) reconstructed in the output plane.

6. Outlook

Laser shadow photography and interferometry are universal tools for studying the fine-structured electrical spark. However, the complexity of this three-dimensional plasma object naturally limits the accuracy of its precise investigation by the mentioned methods. Complicated interference effects, occurring at beam transmission through the complex spark, give rise to multiple zones with fine-scale beats in the radiation intensity and phase shift distributions. To reliably resolve these beats, objectives with a spatial resolution close to several micrometers are required (see the simulated results in Figs. 9 and 10). Otherwise, distorted spark patterns will be registered; multiple small-scale beats of the radiation intensity and phase shift distributions will be smoothed. Registration of fine-scale beats of the radiation intensity and phase shift is of vital importance for analyzing diffraction of laser radiation by a complex three-dimensional plasma object in the framework of solving the direct and inverse wave-scattering problems (see in [28–30]). The latter are crucial for reconstructing the spark characteristics (diameters and number of filaments, their packing density in the channel cross-section, electron density distributions for single filaments, etc.). At the same time, we do not exclude the possibility that the real spark patterns can contain structures finer (with sizes about several micrometers) than those registered in the experiment. Such structures can be unresolved even by the employed optics. Apart from high-performance characteristics, the employed objectives should additionally have a large working distance (when the entrance pupil is located far from the spark) to provide for safe imaging of the spark. The spark self-radiation and the shock wave generated at the post-stage of the discharge can damage the surface of the entrance lens. Consequently, to reliably register the spark patterns, specialized optics is required.

In order to analyze the radiation diffraction by a complex-structured spark, one should reconstruct the radiation characteristics in the output plane (Fig. 5) of the spark by using the registered shadowgram and interferogram. If the object plane of the objective coincides with the output plane of the spark, the objective defocusing can be neglected. However, the sporadic development of the spark in space and the necessity for scaling the registered images imply the employment of a certain reference object, on which the optical setup is focused. The object should have calibrated dimensions, and its position relative to the output plane of the spark should be known. In this regard, the employment of a thin electrode greatly simplifies the problem and provides a means to account for the defocusing effect with reliable accuracy.

The accuracy of reconstructing the radiation characteristics in the output plane of the spark depends on the accuracy of determining the position of this plane relative to the object plane of the objective (see Figs. 7 and 8). For more accurate determination of the position of the output plane in each spark channel cross-section, one can implement simultaneous two-angle laser probing (i.e. two beams transmitted through the spark at 90°) supplemented with additional schlieren imaging [31]. This technique is sensitive to low gradients of the plasma refractive index and can help in resolving the spark structures at the periphery of the resultant channel, which are poorly visible in interferograms and shadowgrams. Alternatively, instead of seeking for the most probable position of the output plane, one can accurately reconstruct the radiation characteristics in some plane separated from the object plane by a distance taken a-priori greater than the spark channel radius in the considered section. In this case, the distance between the noted planes serves as an independent parameter in the radiation diffraction problem. By optimizing this parameter, one can find the best correlation between the simulated results and the experimental data.

Modeling has shown that the radiation intensity distribution is highly susceptible to distortions introduced by the defocusing effect. In contrast, the phase shift distribution suffers less from this effect. Under our experimental conditions, one can expect the resultant error of reconstructing the spark phase pattern in the output plane to be below 20%, although this error is even smaller on average (see Fig. 8). We believe that, with very accurate objective focusing on the pin electrode,

the resultant error of reconstructing the phase shift distribution can be significantly reduced. The final stumbling block, of course, is the objective resolution. So, when solving the inverse diffraction problem, processing of the spark phase pattern can be the key to approaching the true spark characteristics with good accuracy.

Disclosures. The authors declare no conflicts of interest.

Data availability. Data underlying the results presented in this paper are not publicly available at this time but may be obtained from the authors upon reasonable request.

References

1. K. I. Almazova, A. N. Belonogov, V. V. Borovkov, E. V. Gorelov, I. V. Morozov, A. A. Tren'kin, and S. Y. Kharitonov, "Microstructure of a Spark Discharge in Air in a Point-Plane Gap," Tech. Phys. **63**(6), 801–805 (2018).
2. K. I. Almazova, A. N. Belonogov, V. V. Borovkov, Z. R. Khalikova, G. B. Ragimkhanov, D. Tereshonok, and A. A. Trenkin, "Investigation of plasma properties in the phase of the radial expansion of spark channel in the pin-to-plate geometry," Plasma Sources Sci. Technol. **30**(9), 095020 (2021).
3. K. I. Almazova, A. N. Belonogov, V. V. Borovkov, V. S. Kurbanismailov, Z. R. Khalikova, P. K. Omarova, G. B. Ragimkhanov, D. V. Tereshonok, and A. A. Trenkin, "Investigation of the microchannel structure in the initial phase of the discharge in air at atmospheric pressure in the "pin (anode)-plane" gap," Phys. Plasmas **27**(12), 123507 (2020).
4. K. I. Almazova, A. N. Belonogov, V. V. Borovkov, V. S. Kurbanismailov, G. B. Ragimkhanov, A. A. Tren'kin, D. V. Tereshonok, and Z. R. Khalikova, "Plasma and Gas-Dynamic Near-Electrode Processes in the Initial Phase of a Microstructured Spark Discharge in Air," Tech. Phys. Lett. **46**(8), 737–740 (2020).
5. E. V. Parkevich, M. A. Medvedev, A. I. Khirianova, G. V. Ivanenkov, A. S. Selyukov, A. V. Agafonov, K. V. Shpakov, and A. V. Oginov, "Extremely fast formation of anode spots in an atmospheric discharge points to a fundamental ultrafast breakdown mechanism," Plasma Sources Sci. Technol. **28**(12), 125007 (2019).
6. E. V. Parkevich, M. A. Medvedev, G. V. Ivanenkov, A. I. Khirianova, A. S. Selyukov, A. V. Agafonov, P. A. Korneev, S. Y. Gus'kov, and A. R. Mingaleev, "Fast fine-scale spark filamentation and its effect on the spark resistance," Plasma Sources Sci. Technol. **28**(9), 095003 (2019).
7. E. V. Parkevich, M. A. Medvedev, A. S. Selyukov, A. I. Khirianova, A. R. Mingaleev, S. N. Mishin, S. A. Pikuz, and A. V. Oginov, "Setup involving multi-frame laser probing for studying fast plasma formation with high temporal and spatial resolutions," Opt. Lasers Eng. **116**, 82–88 (2019).
8. A. A. Tren'kin, K. I. Almazova, A. N. Belonogov, V. V. Borovkov, E. V. Gorelov, I. V. Morozov, and S. Y. Kharitonov, "Dynamics of the Initial Stage of the Spark and Diffuse Discharges in Air in a Point-Plane Gap at Different Parameters of the Tip Electrode," Tech. Phys. **64**(4), 470–474 (2019).
9. K. I. Almazova, A. N. Belonogov, V. V. Borovkov, E. V. Gorelov, I. V. Morozov, A. A. Tren'kin, and S. Y. Kharitonov, "Investigation of Spark Discharge Dynamics in an Air-Filled Point-Plane Gap by Shadow Photography," Tech. Phys. **64**(1), 61–63 (2019).
10. E. V. Parkevich, A. I. Khirianova, A. V. Agavonov, S. I. Tkachenko, A. R. Mingaleev, T. A. Shelkovenko, A. V. Oginov, and S. A. Pikuz, "Anode Plasma Formation at the Initial Stage of a Nanosecond Air Discharge," J. Exp. Theor. Phys. **126**(3), 422–429 (2018).
11. J. Goodman, *Introduction to Fourier Optics* (Stanford University, 2005).
12. H. H. Hopkins, *Wave theory of aberrations* (Clarendon, 1950).
13. A. R. FitzGerrell, E. R. Dowski, and W. T. Cathey, "Defocus transfer function for circularly symmetric pupils," Appl. Opt. **36**(23), 5796–5804 (1997).
14. H. H. Hopkins, "The Use of Diffraction-based Criteria of Image Quality in Automatic Optical Design," Opt. Acta **13**(4), 343–369 (1966).
15. H. H. Hopkins and C. R. Burch, "The frequency response of a defocused optical system," Proc. R. Soc. Lond. A **231**(1184), 91–103 (1955).
16. M. Born and E. Wolf, *Principles of Optics* (Cambridge University, 1999).
17. E. V. Parkevich, M. A. Medvedev, A. S. Selyukov, A. I. Khirianova, A. R. Mingaleev, and A. V. Oginov, "Laser-triggered gas switch with subnanosecond jitter and breakdown delay tunable over ~0.1-10 ns governed by the spark gap ignition angle," Plasma Sources Sci. Technol. **29**(5), 05LT03 (2020).
18. E. V. Parkevich, G. V. Ivanenkov, M. A. Medvedev, A. I. Khirianova, A. S. Selyukov, A. V. Agafonov, A. R. Mingaleev, T. A. Shelkovenko, and S. A. Pikuz, "Mechanisms responsible for the initiation of a fast breakdown in an atmospheric discharge," Plasma Sources Sci. Technol. **27**(11), 11LT01 (2018).
19. G. S. Sarkisov, "Shearing interferometer with an air wedge for the electron density diagnostics in a dense plasma," Instrum. Exp. Tech. **39**(5), 727–731 (1996).

20. S. A. Pikuz, V. M. Romanova, N. V. Baryshnikov, M. Hu, B. R. Kusse, D. B. Sinars, T. A. Shelkovenko, and D. A. Hammer, "A simple air wedge shearing interferometer for studying exploding wires," Rev. Sci. Instrum. **72**(1), 1098–1100 (2001).

21. S. A. Pikuz, "Reply to Some critical remarks about the paper, 'A simple air wedge shearing interferometer for studying exploding wires'," Rev. Sci. Instrum. **74**(6), 3192–3193 (2003).

22. D. S. Volosov, *Photographic optics* (Iskusstvo, 1978). In Russian.

23. A. Khirianova, E. Parkevich, M. Medvedev, K. Smaznova, T. Khirianov, E. Varaksina, and A. Selyukov, "Extraction of high-contrast diffraction patterns of fine-structured electrical sparks from laser shadowgrams," Opt. Express **29**(10), 14941–14962 (2021).

24. I. Gurov and M. Volkov, "Fringe Evaluation and Phase Unwrapping of Complicated Fringe Patterns by the Data-Dependent Fringe Processing Method," IEEE Trans. Instrum. Meas. **55**(5), 1634–1640 (2006).

25. C. J. R. Sheppard, "Depth of field in optical microscopy," J. Microsc. **149**(1), 73–75 (1988).

26. S. A. Rodionov, *The automation of the design of optical systems* (Mashinostroenie, 1982). In russian.

27. H. H. Hopkins, "Canonical Pupil Coordinates in Geometrical and Diffraction Image Theory," Jpn. J. Appl. Phys. **3**(S1), 31 (1964).

28. P. Müller, M. Schürmann, and J. Guckmuller, "The theory of diffraction tomography," 2015, Https://arxiv.org/abs/1507.00466.

29. D. L. Marks, "A family of approximations spanning the Born and Rytov scattering series," Opt. Express **14**(19), 8837–8848 (2006).

30. Y. Sung, W. Choi, C. Fang-Yen, K. Badizadegan, R. R. Dasari, and M. S. Feld, "Optical diffraction tomography for high resolution live cell imaging," Opt. Express **17**(1), 266–277 (2009).

31. P. K. Panigrahi, *Schlieren and Shadowgraph Methods in Heat and Mass Transfer* (Springer-Verlag, 2012).